2014

Investigation of Cyclic Liquefaction with Discrete Element Simulations

Matthew R. Kuhn
University of Portland, kuhn@up.edu

Hannah E. Renken

Austin D. Mixsell

Steven L. Kramer

Investigation of Cyclic Liquefaction with Discrete Element Simulations

Matthew R. Kuhn, M.ASCE[1]; Hannah E. Renken[2]; Austin D. Mixsell[3]; and Steven L. Kramer, M.ASCE[4]

Abstract: A discrete-element method (DEM) assembly of virtual particles is calibrated to approximate the behavior of a natural sand in undrained loading. The particles are octahedral, bumpy clusters of spheres that are compacted into assemblies of different densities. The contact model is a Jäger generalization of the Hertz contact, which yields a small-strain shear modulus that is proportional to the square root of confining stress. Simulations made of triaxial extension and compression loading conditions and of simple shear produce behaviors that are similar to sand. Undrained cyclic shearing simulations are performed with nonuniform amplitudes of shearing pulses and with 24 irregular seismic shearing sequences. A methodology is proposed for quantifying the severities of such irregular shearing records, allowing the 24 sequences to be ranked in severity. The relative severities of the 24 seismic sequences show an anomalous dependence on sampling density. Four scalar measures are proposed for predicting the severity of a particular loading sequence. A stress-based scalar measure shows superior efficiency in predicting initial liquefaction and pore pressure rise. **DOI: 10.1061/(ASCE)GT.1943-5606.0001181.**

Author keywords: Liquefaction; Discrete-element method (DEM); Contact mechanics; Simulation; Undrained loading.

Introduction

Cyclic liquefaction is commonly thought to develop from the microscale jostling of particles during repeated load reversals or rotations of the principal stresses, which causes a progressive rearrangement of the particles and a tendency of the soil to contract. This tendency, under undrained conditions, produces positive pore pressure, which leads to a reduction in effective stress and a diminished capacity of the particles to sustain load. In the context of understanding soil behavior at the microscale, rather than at the metascale of continuum constitutive approaches, the micro-level basis of liquefaction was confirmed in the particle-scale, discrete-element method (DEM) simulations of Hakuno and Tarumi (1988) and Dobry and Ng (1992). Because they are more than 20 years old, these simulations of two-dimensional arrays of disks and spheres may seem inelegant by current standards, but they give a convincing demonstration of the microscale origin of cyclic loading behavior: pore pressure rise concurrent with loading and a degradation of the shear modulus with increasing strain magnitude. In a later series of two-dimensional simulations, Ashmawy et al. (2003) produced realistic liquefaction curves, providing the relationship between cyclic stress amplitude and the number of cycles to failure. Other simulations have shown that the load-bearing capacity of a granular material is diminished during repeated loading, reducing the number of interparticle contacts, leading to pore pressure rise under undrained conditions, and altering the fabric anisotropy (Ng and Dobry 1994; Sitharam 2003; Sazzad and Suzuki 2010). Recently, the interplay of pore fluid and grains has been simulated by coupling DEM with discretized Navier-Stokes models, permitting the simulation of entire soil strata to track the progression of larger-scale phenomena (e.g., lateral spreading) and the upward migration of water during ground shaking.

The present work uses the DEM to explore the cyclic liquefaction behavior of a target sand (Nevada sand) by attempting a modest fidelity to its measured, laboratory behavior. After showing that the model captures many aspects of this sand's behavior, the model is used to simulate conditions that can occur in the field, but which are difficult to manage in a laboratory setting. A predictive measure of loading conditions conducive to liquefaction is obtained.

The DEM simulations in this study used the open source *OVAL* code (Kuhn 2002) and are element tests in which small assemblies of particles in a box undergo various deformation sequences. The purpose is to explore the material behavior of a simulated soil element, which represents an idealized material point in a soil continuum or an integration point in a finite- element model, rather than study a larger boundary value problem [e.g., a footing foundation or an entire soil column, as was done by El Shamy and Zamani (2012) and El Shamy and Zeghal (2005)]. Fig. 1 shows an assembly of 6,400 particles that represents a small soil element of size $18 \times 12 \times 12\, D_{50}$ (approximately $3 \times 2 \times 2$ mm); this is large enough to capture the average material behavior but sufficiently small to prevent mesoscale localization, such as shear bands, or the macroscale nonuniformities produced by boundary conditions (footings, excavations, etc.). In this work, certain advantages of DEM simulations are used for exploring material behavior. Once a DEM assembly is created, the same assembly can be reused with loading sequences of almost unlimited variety, all beginning from precisely the same particle arrangement, during which all Cartesian components of stress and strain are accessible. The DEM tests also permit loading sequences with arbitrary control of any six components of

[1]Professor, Dept. of Civil Engineering, Donald P. Shiley School of Engineering., Univ. of Portland, Portland, OR 97203 (corresponding author). E-mail: kuhn@up.edu

[2]Civil Engineer, Federal Aviation Administration (FAA), Renton, WA 98057; formerly, Research Student, Univ. of Portland, Portland, OR 97203.

[3]Civil Engineer, Western Service Area (WSA), Navigational Aids Engineering Center (NAVAIDS), Federal Aviation Administration (FAA), Renton, WA 98057; formerly, Research Student, Univ. of Portland, Portland, OR 97203.

[4]John R. Kiely Professor of Civil and Environmental Engineering, Dept. of Civil and Environmental Engineering, Univ. of Washington, Seattle, WA 98195. E-mail: kramer@u.washington.edu

Note. This manuscript was submitted on October 8, 2013; approved on July 23, 2014; published online on September 8, 2014. Discussion period open until February 8, 2015; separate discussions must be submitted for individual papers. This paper is part of the ***Journal of Geotechnical and Geoenvironmental Engineering***, © ASCE, ISSN 1090-0241/04014075(13)/$25.00.

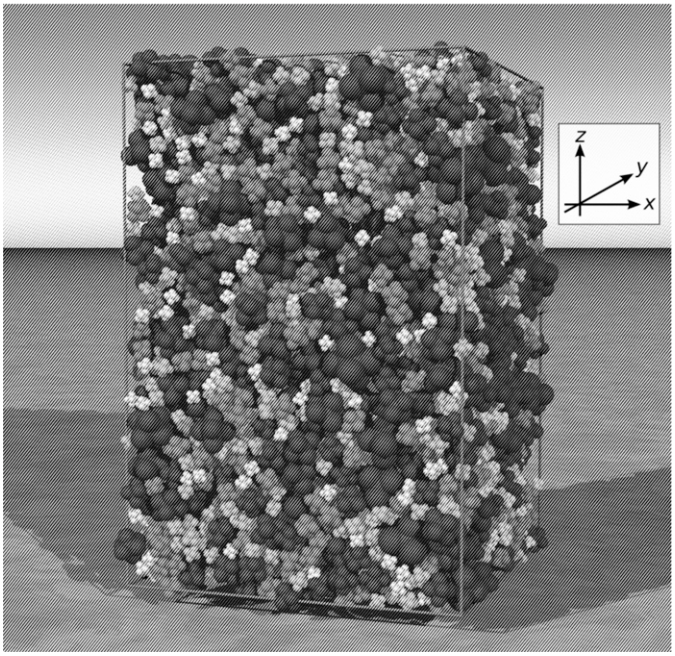

Fig. 1. DEM assembly of 6,400 particles

the stress and strain rates or of their linear combinations, which are loading conditions that could require a different testing apparatus in a physical laboratory. The average stress within an assembly is computed from the intergranular contact forces, so that the computed stresses are inherently effective stresses.

The following section presents details of the DEM model, focusing on refinements to current models. This section is followed by presentations of the model's monotonic and cyclic loading behaviors. The cyclic response is explored for level-ground conditions of cyclic simple shear, in which shear stress is applied in three types of sequences: uniform-amplitude loading, nonuniform amplitude sequences, and realistic seismic loading sequences. These simulations are used to evaluate proposed severity measures for predicting the onset of liquefaction.

Granular Assembly

The DEM assemblies (Fig. 1) were constructed with the goal of approximating the behavior of Nevada sand, a standard, poorly graded sand (SP) used in laboratory and centrifuge testing programs, including the Verification of Liquefaction Analysis by Centrifuge Studies (VELACS) program (Arulanandan and Scott 1993; Arulmoli et al. 1992; Cho et al. 2006; Duku et al. 2008). A DEM model can be customized by adjusting several characteristics, including (1) particle size and size distribution, (2) particle shape, (3) compaction procedure, (4) the contact force-displacement relation, and (5) the contact friction coefficient. At the outset, it was recognized that a DEM model is unlikely to reproduce all of the behaviors of a targeted soil. The following modest goals were set relative to Nevada sand: similarities in particle size distribution, range of void ratios, small-strain stiffness, and the critical state (CS) friction angle.

Attaining the desired median particle size $D_{50} = 0.165$ mm is a simple matter of scaling the DEM particles; however, fashioning the size distribution involves some compromise because computation time is favored by a smaller range of particle sizes. For this reason, particle sizes were selected to fit the central portion of the particle size distribution of Nevada sand (Fig. 2) by neglecting the smallest and largest 3.5% of sizes.

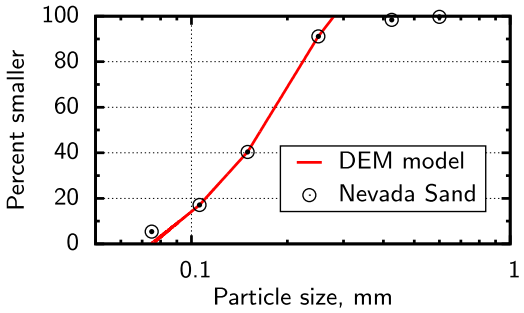

Fig. 2. Particle size distributions

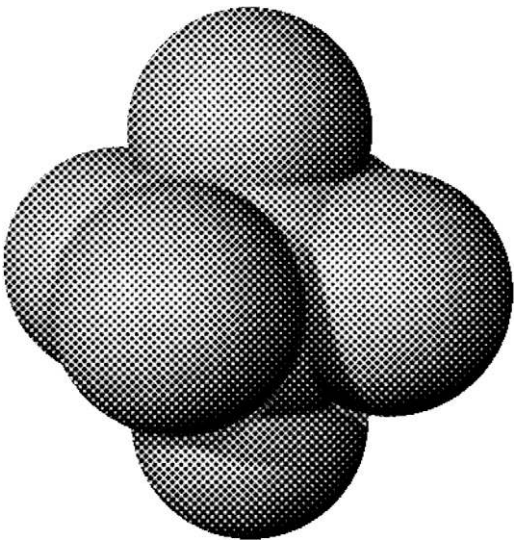

Fig. 3. Particle shape: a bumpy octahedral cluster of spheres

An assembly of spheres cannot adequately represent a natural sand; sphere packings have a narrow range of void ratios (typically $e = 0.55-0.73$ for glass ballotini) (Zettler et al. 2000). A sphere can touch a neighboring sphere only at a single contact, and sphere assemblies have relatively low strength (a friction angle ϕ of approximately 20°) (Cho et al. 2006). To achieve more realistic simulations, a bumpy, compound cluster shape with a large central sphere with six embedded satellite spheres in an octahedral arrangement was chosen (Fig. 3). Together with its computational advantages, the shape is sufficiently nonround to produce a large range of initial densities, and the basic shape can be modified to attain a targeted range of densities (i.e., the relative radii of the single central sphere and the outer satellite spheres, as well as the relative protrusions of the outer spheres, can be modified). The work of Cho et al. (2006) was used for guidance; these researchers developed correlations between a sand's particle shape and its strength and density range. Salot et al. (2009) studied the effects of DEM particle shape and contact friction on density and strength, and they developed a procedure for calibrating a DEM assembly to approximate the behavior of a targeted sand. With this guidance and considerable trial and error, a shape that produced a realistic strength and range of void ratios was produced as described in the following. This shape has a ratio of central-to-satellite sphere radii of 0.75, and the satellite spheres were centered at octahedral points located at 0.925 of the radius of the inner sphere from its center (Fig. 3).

In a laboratory setting, sand can be conditioned, placed, and compacted in various ways to produce a desired density and fabric.

Because many of these laboratory procedures cannot yet be simulated, a simpler computational procedure is used, which produces assemblies with a similar range of densities as Nevada sand and with a modest fabric anisotropy, as would be expected with a laboratory pluviation procedure. To start, the 6,400 particles were sparsely and randomly arranged within a spatial cell surrounded by periodic boundaries. In the absence of gravity and with a reduced interparticle friction coefficient ($\mu = 0.30$), the assembly was anisotropically (uniaxially) compacted by slowly reducing its height, but with no lateral strain. The initially sparse arrangement with zero stress eventually seizes when a loose yet load-bearing fabric is formed. A series of 14 progressively denser assemblies were created by repeatedly assigning random velocities to particles of the previous assembly (simulating a disturbed or vibrated state), and then further reducing the assembly height until the newer specimen seizes again. The 15 specimens had void ratios in the range e_{loosest} to e_{densest} of 0.850 to 0.525, a range that is similar to that of Nevada sand obtained with standard ASTM procedures [standards D4253 (ASTM 2006a) and D4254 (ASTM 2006b)]. Although the authors do not contend that virtual specimens with a range e_{loosest} to e_{densest} correspond to the range $e_{\max}$ to $e_{\min}$ attained with ASTM procedures, some auxiliary evidence does support a similarity in the two ranges. Attempting to simulate glass ballotini, the same DEM procedure was applied to create assemblies of spherical particles with a narrow range of diameters. The simulated compaction procedure results in assemblies with the range e_{loosest} to e_{densest} of 0.750 to 0.549, which compares favorably with ranges $e_{\max}$ to $e_{\min}$ that have been reported for ballotini prepared with the ASTM procedures (approximately 0.73–0.58) (Zettler et al. 2000).

Having created 15 assemblies with this anisotropic compaction scheme, the friction coefficient μ was raised to 0.60, and each assembly was isotropically consolidated to a mean effective stress of 10 kPa. This step simulates the isotropic consolidation of a pluviated sample, as in standard triaxial testing, and leaves the sample with a small initial anisotropy (a Satake fabric anisotropy $F_{zz}/F_{xx} = 1.08$). Most results in this work involve a further isotropic consolidation to the higher stress of 80 kPa, so that results can be compared with the Nevada sand tests by Arulmoli et al. (1992). In short, the preparation initially created assemblies with an anisotropic fabric at low stress, followed by isotropic consolidation to a mean effective stress of 10 kPa or higher.

The small-strain behavior of a DEM assembly is sensitive to the particular force-displacement model of the contacts. During cyclic loading of a sand, the mean effective stress p can be progressively reduced to nearly zero, and further cyclic loading causes p to rise and fall across a broad range of values. It is believed that the proper simulation of liquefaction requires a contact model that appropriately reflects a sand's small-strain material behavior over a range of p. As a minimum, the relationship between the small-strain bulk shear modulus $G_{\max}$ and the mean effective stress p should comport with that of sand. The modulus $G_{\max}$ of sands is usually found to vary in proportion to p^{β}, where exponent β is in the range 0.4–0.6, depending on the particle shape (Cho et al. 2006), the particle size gradation (Wichtmann and Triantafyllidis 2009), surface roughness (Santamarina and Cascante 1998), and preload conditioning. A β of 0.5 is commonly used in geotechnical practice and for correlations between $G_{\max}$, e, and p (Hardin 1978). An exponent of 0.5 also fits the data for Nevada sand (Arulmoli et al. 1992) and was the targeted exponent in this work.

From a micromechanics viewpoint, exponent β is known to depend upon the contact stiffnesses of particle pairs (Walton 1987; Goddard 1990; Agnolin and Roux 2007). Most DEM simulations use a standard Hertz-Mindlin contact model in which particles touch at spherical surfaces and behave as elastic bodies. This contact model gives a normal force f^n that is proportional to the normal contact indentation ζ raised to the power $3/2$ as $f^n \propto \zeta^{3/2}$. The bulk stiffness of a granular assembly can be estimated from a simple idealization in which all contacts bear an equal force and the particle-scale displacement field conforms with the bulk field. This simple model predicts an exponent $\beta = 1/3$, such that $G_{\max} \propto p^{1/3}$ (Walton 1987). Simulations of sphere assemblies, in which these simplifying assumptions are removed, yield somewhat greater exponents β (Agnolin and Roux 2007), and the DEM simulations of sphere assemblies in this work give the proportionality $G_{\max} \propto p^{0.42}$ (Table 1, row 2). Simulations with the bumpy clusters of Figs. 1 and 3 give $G_{\max} \propto p^{0.39}$ (Table 1, row 3). In these simulations, the grains were assigned a shear modulus G_s of 29 GPa and a Poisson's ratio ν_s of 0.15, which are values that lie within the range of quartz (Simmons and Brace 1965; Mitchell and Soga 2005). A friction coefficient $\mu = 0.60$, also within the range of quartz, was chosen to fit the behavior of Nevada sand (Mitchell and Soga 2005). Simulation values

Table 1. Effect of the Contact Profile and Particle Shape on Small-Strain Bulk Stiffness $G_{\max}$ and Exponent β (as $G_{\max} \propto p^{\beta}$)

Row	Particle shape	Contact contour	Source	A_α	$G_{\max}$ (MPa) at $p = 80$ kPa	Exponent β
1	Spheres	Spherical ($\alpha = 2$)	Theory[c]	$1/2R$	180[c]	0.33
2	Spheres[a]	Spherical ($\alpha = 2$)	DEM	$1/2R$	118	0.42
3	Sphere clusters[b]	Spherical ($\alpha = 2$)	DEM	$1/2R$	170	0.39
4	Spheres[a]	Conical ($\alpha = 1$)	Theory[d]	0.050[d]	142[d]	0.50
5	Spheres	Conical ($\alpha = 1$)	DEM	0.050	138	0.56
6	Sphere clusters[b]	Conical ($\alpha = 1$)	DEM	0.070	89.6	0.56
7	Sphere clusters[b]	$\alpha = 1.3$	DEM	5.3[e]	90.2	0.50
8	Sphere clusters[b]	$\alpha = 0.8$	DEM	0.0045[e]	90.2	0.60
9	Sphere clusters[b]	$\alpha = 2.1$	DEM	5.5×10^{5}[e]	89.6	0.40
10	Sand	—	Experiment	—	71–96[f]	0.4–0.6[g]

[a]DEM assembly of 6,400 spheres with $e = 0.538$, $G_s = 29 \times 10^9$ GPa, and $\nu_s = 0.15$.

[b]Figs. 1 and 3. Assembly of 6,400 particles with $e = 0.638$, $G_s = 29 \times 10^9$ GPa, and $\nu_s = 0.15$.

[c]See Walton (1987). An estimate of $G_{\max}$ depends upon packing characteristics. The values shown correspond to packing conditions of row 2.

[d]See Goddard (1990). An estimate of $G_{\max}$ depends upon packing characteristics. The values shown correspond to the packing characteristics of the assembly in row 2.

[e]A_α chosen to yield $G_{\max} \approx 90$ MPa. Values of A_α have dimensional units ($m^{1-\alpha}$).

[f]Resonant column testing of Nevada sand (Specimen 60-43, $e = 0.659$, $\gamma = 0.001\%$, $G_{\max} = 71$ MPa) (Arulmoli et al. 1992); correlations of Hardin (1978) ($e = 0.638$, $p = 80$ kPa, $G_{\max} = 88$ MPa) and correlations of Wichtmann and Triantafyllidis (2009) ($e = 0.638$, $C_u = 2.1$, $p = 80$ kPa, $G_{\max} = 96$ MPa). See also Pestana and Whittle (1995).

[g]See Cho et al (2006) and Wichtmann and Triantafyllidis (2009). For Nevada sand, $\beta = 0.5$ (Arulmoli et al. 1992), Specimen 60-43.

of bulk stiffness G_{max} were measured at shear strain $\gamma = 0.001\%$. These values were compared with those of laboratory resonant column tests of Nevada sand and correlations gained from various sands, which gave $G_{max} = 71-96$ MPa (Table 1, row 10 and footnotes f and g). In short, simulations with the standard Hertz-Mindlin contact model yield a poor match with the exponent β and overpredict G_{max} for the range of pressures that typically apply in field liquefaction situations.

Goddard (1990) noted that a larger exponent β is obtained if the particles interact at conical asperities rather than along ideally smooth spherical surfaces [Fig. 4(b)]. He arrived at an exponent $\beta = 1/2$ (as $G_{max} \propto p^{1/2}$) by applying the same simplifying assumptions that lead to a value of $1/3$ for spherical contacts. In this work, the DEM simulations with assemblies of spheres and of sphere clusters with conical asperities give an exponent β of 0.56 (Table 1, rows 4 and 5), which overpredicts the target value of $\beta = 0.50$ with both particle shapes.

Although the true nature of contact between natural sand particles is currently a matter of intense interest (Cavarretta et al. 2010; Cole et al. 2010), their contact surfaces are certainly not glassy smooth spheres. A technique was used in which contacts were numerically detected at the smooth spherical lobes of the bumpy clusters (Fig. 3), whereas contact forces were computed by assuming rounded, but nonspherical, asperities of approximately 1-μm width. Jäger (1999) derived the normal force f^n between an asperity of a general form (i.e., a solid of revolution with the power-form surface contour $z = A_\alpha r^\alpha$, for a positive α) and a hard flat surface [see Fig. 4(a)]

$$f^n = C_\alpha \zeta^{1+1/\alpha}, \quad C_\alpha = \frac{4\alpha G_s}{(1-\nu_s)(1+\alpha)} \left(\frac{\Gamma\left(\frac{1+\alpha}{2}\right)}{\sqrt{\pi} A_\alpha \Gamma\left(\frac{2+\alpha}{2}\right)} \right)^{1/\alpha} \tag{1}$$

where ζ = indentation depth (half of the contact overlap); G_s and μ_s = shear modulus and Poisson's ratio of the solid grains, respectively; and Γ = gamma function. For smooth spherical surfaces that conform with a particle's radius R, the exponent α is 2, and the contour parameter A_2 is $1/(2R)$, so that Eq. (1) yields the standard Hertz solution

$$C_2 = \frac{8}{3} \frac{G_s}{1-\nu_s} R^{1/2}, \quad f^n = \frac{8}{3} \frac{G_s}{1-\nu_s} R^{1/2} \zeta^{3/2} \tag{2}$$

With a conical asperity [$\alpha = 1$; Fig. 4(b)], A_1 corresponds to the outer slope of the cone, and

$$C_1 = \frac{4G_s}{\pi(1-\nu_s)} \frac{1}{A_1}, \quad f^n = \frac{4G_s}{\pi(1-\nu_s)} \frac{1}{A_1} \zeta^2 \tag{3}$$

By decoupling the asperity shape from the more general contour of a particle's surface, Eqs. (1) and (3) afford a free parameter A_α that can be chosen so that the DEM assembly has a G_{max} similar to that of a targeted sand.

To produce simulations in which exponent $\beta = 0.50$ and $G_{max} \propto p^{0.50}$, an asperity contour with parameter $\alpha = 1.3$ [Eq. (1)] was used, which forms a rounded cone whose surface lies between spherical and conical contours [Table 1, row 7, and Fig. 4(c)]. The value 1.3 was chosen through trial and error, with the corresponding parameter $A_{1.3}$ chosen so that G_{max} is close to the target value of 90 MPa at a mean effective stress of 80 kPa. The simulations in this work use this pair of values, α and A_α. For particles of sub-millimeter size, such as in Nevada sand [Eq. (1)], these conditions imply an indentation depth of the asperities of a few tens of nanometers (approximately 0.05 μm for $p = 80$ kPa) and a width of approximately 1 μm [Fig. 4(c)]. Alternative pairs of values α and A_α, with shapes that are more rounded and more pointed [Table 1, rows 8 and 9, and Fig. 4(c)], yield the exponents $\beta = 0.40$ and 0.60, respectively, which encompasses the range of small-strain behaviors that have been measured with sands (e.g., Table 1, footnote f).

A DEM simulation must also compute the tangential forces between particles, accounting both for elastic effects and for the frictional limit of force. Although tangential contact motion is often idealized as advancing steadily across a particle's surface, DEM simulations reveal that tangential motions are quite irregular and errant, and that the normal force will irregularly increase and decrease during the concurrent tangential motion (Kuhn 2011). The calculation of tangential force between DEM particles must account for the complex elastic-frictional response during such irregular motions, particularly when an assembly undergoes realistic seismic loading. The tangential contact forces were calculated with an extension of the Hertz-Mindlin-Deresiewicz theory (Mindlin and Deresiewicz 1953) by using the more general Jäger contact algorithm (Jäger 2005; Kuhn 2011). This algorithm fully accounts for arbitrary sequences of normal and tangential contact movements in a three-dimensional setting while maintaining the objectivity of the resulting contact forces. [The pseudocode in Kuhn (2011) requires the modification of only two lines, 13 and 42, to accommodate the general Eq. (1).]

Monotonic Loading

Before conducting cyclic tests, the DEM model was calibrated and verified by comparing its monotonic undrained loading behavior with that of Nevada sand. These tests were used to select the interparticle friction coefficient, $\mu = 0.60$. Fig. 5 shows the stress paths

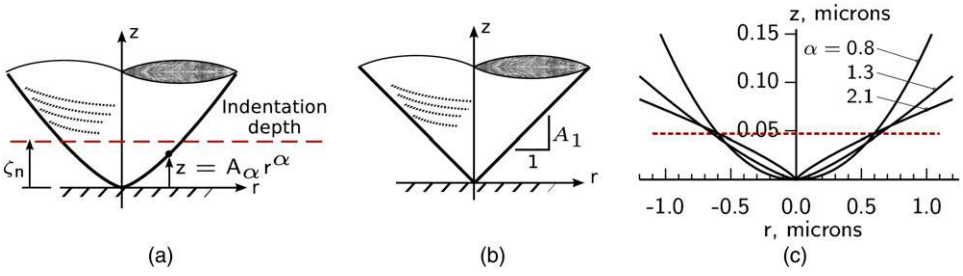

Fig. 4. Contours of contact asperities as power-law surfaces of revolution: (a) general power-law form with exponent α and parameter A_α; (b) conical asperity; (c) asperity used in the DEM simulations (labeled $\alpha = 1.3$)

J. Geotech. Geoenviron. Eng., 2014, 140(12): 04014075

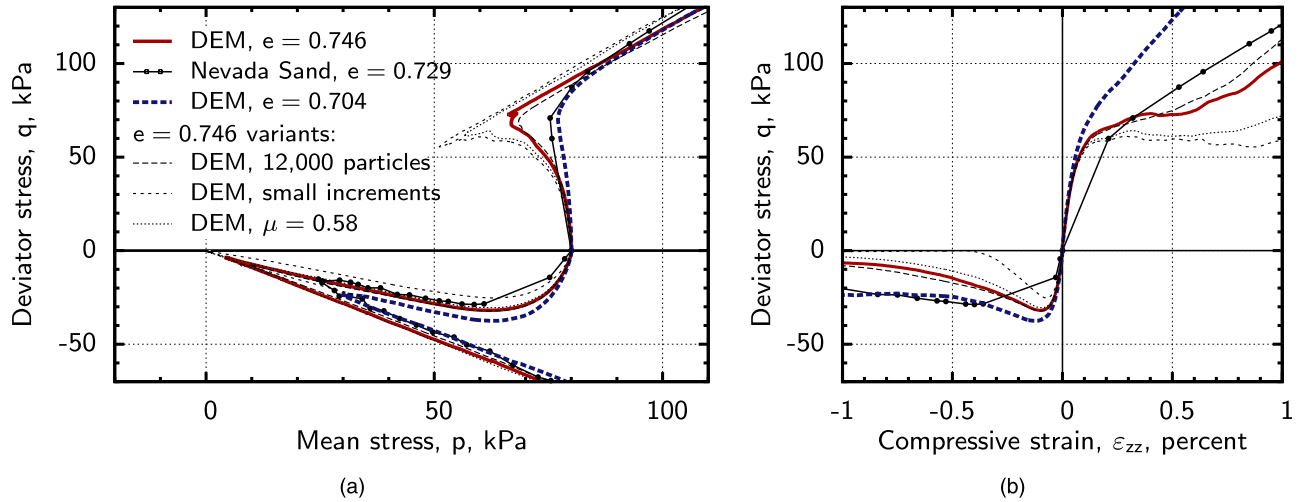

Fig. 5. Undrained triaxial compression and extension of DEM simulations and Nevada sand tests (CIUC40-04 and CIUE40-12 are shown) (data from Arulmoli et al. 1992): (a) stress paths; (b) stresses and strains

of undrained triaxial compression and extension simulations with assemblies that have void ratios of 0.704 and 0.746, as well as a laboratory test of Nevada sand with a void ratio of 0.734 [the $D_r = 40\%$ tests of Arulmoli et al. (1992)]. Heavier lines in Fig. 5 are for simulations conducted under the previously described conditions and presented throughout most of this work. Thinner lines are for variations of these conditions discussed in the following. In typical undrained laboratory tests, the pore fluid is entrapped within a saturated soil sample, preventing volume change during loading. The DEM model contains no interstitial fluid; instead, undrained, zero volume-change conditions are created by prescribing normal strains in the three coordinate directions: $(1+\varepsilon_{xx})(1+\varepsilon_{yy})(1+\varepsilon_{zz}) = 1$ (Fig. 1). The DEM assembly was consolidated from the initial mean effective stress of 10 kPa to a mean stress $p_o = 80$ kPa, and the subsequently induced pore-water pressure was computed from measured reductions in the mean effective stress $\Delta u = p_o - p$, where p is directly computed from the interparticle forces.

Loading was applied in the z-direction in a slow, quasi-static manner; movements of the periodic boundaries were much slower than the material's wave speed. As in many DEM simulations, time was used as a surrogate parameter that advances deformation from one integration step to another, with sufficient steps to allow particles to adjust to the advancing deformation, thus economizing the computational run time. A particle density much smaller than that of sand minerals was used in the simulations, which is a common approach in DEM analysis and reduces the number of time steps while maintaining nearly quasi-static conditions (Thornton and Antony 1998; O'Sullivan et al. 2004). Strain increments $\Delta\varepsilon_{zz} = \pm 5 \times 10^{-7}$ in triaxial compression and extension were sufficiently small to maintain an average force imbalance per particle of less than 4×10^{-3} times the average contact force and an average assembly kinetic energy less than 5×10^{-4} of the internal elastic energy. Although nearly quasi-static, the simulations were not rate independent. Reducing the increment $\Delta\varepsilon_{zz}$ in half softened the behavior (Fig. 5, small increments lines). The effect is similar to reducing the friction coefficient μ to 0.58 (Fig. 5). Consistent conditions of the strain increment and friction coefficient were used throughout all of the simulations described in the following. A larger assembly of 12,000 particles was also tested (Fig. 5), but the results are nearly the same as those of the smaller assembly, which is sufficient for modeling undrained behavior.

The two DEM simulations in Fig. 5 (heavy lines) are for specimens that straddle the density of the Nevada sand specimen, and these simulations capture the primary features found in the laboratory tests: strong strain-softening behavior during triaxial extension that is arrested by phase transformation (PT) at a stress $p \approx 25$ kPa. At larger strains [Fig. 5(a)], the stress paths of the simulations converge to roughly the same CS slopes—in both extension and compression—as those of Nevada sand. Because of these similarities, the same DEM parameters were applied in the remaining simulations.

Fig. 6 shows the undrained behavior in simple shear for four DEM assemblies of different densities. These undrained tests started from an isotropic stress state, and the shear strains were advanced monotonically with $\dot{\gamma}_{xz} > 0$ and $\varepsilon_{xx} = \varepsilon_{yy} = \varepsilon_{zz} = \gamma_{xy} = \gamma_{yz} = 0$ (see Fig. 1), as might be applied in hollow-torsion, constant-height undrained laboratory tests. Unlike the triaxial conditions of Fig. 5, the directions of the principal stresses rotated during the shear loading. Markers locate the instability points (circles) at which shear stress τ_{xz} reached a temporary peak and the PT points (squares) at which the vertical effective stress σ'_{zz} was minimum, which is a state commonly ascribed to a transition from compressive to dilatant behavior. The two loosest assemblies have stress paths that display temporary instability, as would be expected with loose dry-pluviated clean sands, and these looser assemblies have more contractive behavior and lower instability and PT points than those of the denser assemblies. An interpreted PT line is shown in Fig. 6(a), although the stress ratios τ_{xz}/σ'_{zz} of the four PT points decrease slightly with increasing assembly density.

In a complementary series of drained simple-shear, constant-σ_{zz} simulations on the same assemblies, transformations from compressive to dilatant behaviors were observed for the three loosest assemblies; this is a transition called the characteristic state (CHS) (Ibsen 1999). The results show that the same stress ratios τ_{xz}/σ'_{zz} apply to both PT and CHS transitions for the three assemblies, although the CHS occurs at larger shear strains. The same drained simple-shear, constant-σ_{zz} simulations were also used to evaluate the CS, a condition that is attained at large strains and at which shearing progresses at constant density and shear stress. The CS was reached at shear strains γ_{xz} greater than 80%, and the corresponding ratio τ_{xz}/σ'_{zz} is shown as the CHS line in Fig. 6(a). The CS void ratio is 0.912, which is much larger (looser)

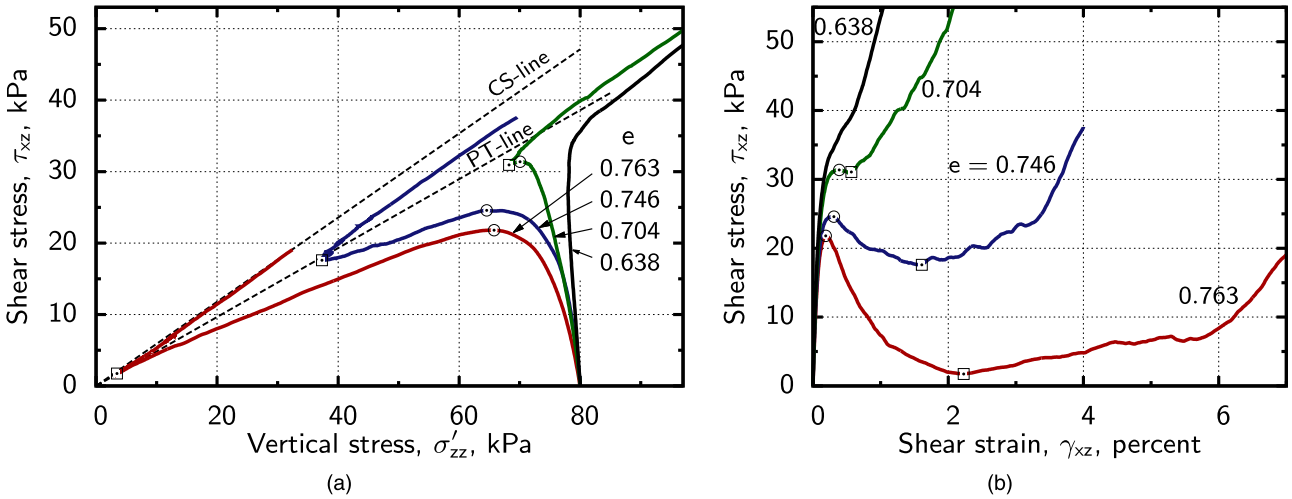

Fig. 6. Undrained monotonic simple shear simulations, showing instability points (circles), PT points (squares), phase-PT line, and CS line: (a) stress paths; (b) shear stress and shear strain

than the initial densities of the four assemblies, a result that is consistent with the PT transition to dilatant behavior observed in the undrained simulations.

Cyclic Simple Shear

Three types of cyclic loading sequences were simulated: (1) uniform amplitude cyclic shearing, (2) alternating and modulated sequences of small and large cyclic amplitudes, and (3) realistic, erratic sequences of seismic shearing. In all cases, cyclic shearing was unidirectional and conducted as undrained simple shear in the horizontal x-direction (i.e., with shearing strains $|\gamma_{xz}| > 0$ and $\gamma_{yz} = \gamma_{xy} = 0$; Fig. 1). As with monotonic loading simulations, the assemblies were consolidated to an isotropic stress of 80 kPa, and undrained conditions were imposed by preventing normal strains in the three coordinate directions, $\varepsilon_{xx} = \varepsilon_{yy} = \varepsilon_{zz} = 0$. No ambient shear stress was imposed, corresponding to level-ground conditions. Pore-water pressure was computed from the measured reductions in mean effective stress, $\Delta u = p_o - p$. This work focuses primarily on four assemblies with a range of void ratios $e = 0.638-0.763$, which corresponds to relative densities D_r in a range of approximately 70–35%.

Uniform Amplitude Cyclic Shearing

Undrained cyclic simple shear loading was applied in a sawtooth manner; a uniform shearing rate $\pm\dot{\gamma}_{xz}$ was imposed in forward and backward directions, reversing the direction each time a target amplitude of shear stress τ_{xz} was reached (Fig. 7). Loading proceeded until the mean effective stress had reached zero—at initial liquefaction—and the total traversed strain $\int |d\gamma_{xz}|$ exceeded 10%. These conditions repeatedly rotated and counterrotated the principal stress directions. The mean stress and shear stress were recorded throughout these strain-controlled histories. The four-way plot in Fig. 8 shows typical results, in this case, with a cyclic stress amplitude $\tau = \pm 13$ kPa [i.e., a cyclic stress ratio (CSR), $\tau_{xz}/p_o = 0.163$]. These plots show the stress path, the stress-strain evolution, and the pore-pressure ratio $r_u = -\Delta u/p_o$, all of which resemble those of saturated sands. The pore pressure increases steadily, and at approximately 10 cycles, the stress path expresses PT behavior (labeled A), whereupon the mean effective stress collapses

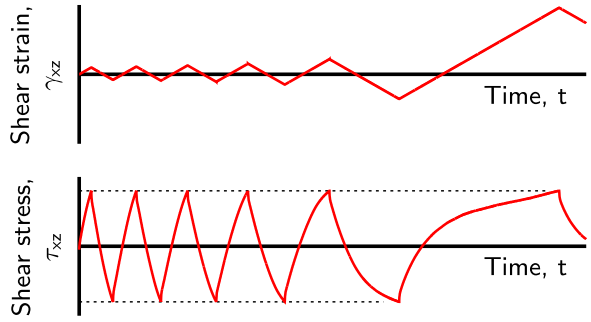

Fig. 7. Loading program for uniform-amplitude cyclic simple shear

to nearly zero. Once PT has occurred, the stress-strain evolution changes from the narrow hysteresis pattern of the first nine cycles (labeled B) into a broader scythe-shaped pattern (labeled C). Initial liquefaction ($r_u = 1.0$) occurs after 10.5 cycles of loading, and a shear strain of 3% is reached at 11 cycles. After liquefaction is initiated, the stress path falls into butterfly repetitions, which is typical of sands (labeled D). These results are qualitatively consistent with undrained cyclic shear tests of sands (Arulmoli et al. 1992; Kammerer et al. 2000; Porcino and Caridi 2007).

Fig. 9 shows the liquefaction curves obtained from multiple simulations of four assemblies with different void ratios. The upward curvature in this semilog plot is similar to that of sands, although the curves have a steeper downward slope than that with most sands (Porcino and Caridi 2007). Confirming the choice of a rounded cone asperity profile (Table 1, row 7), simulations with a standard Hertz-Mindlin spherical contact (Table 1, row 3) yielded an even steeper downward slope: 20–50% more cycles at large shear stress ratios and 20–30% fewer cycles at small ratios. Results were also obtained for a large assembly of 12,000 particles, and the results are nearly indistinguishable from those in Fig. 9.

Nonuniform Cyclic Sequences

Wang and Kavazanjian (1989) conducted experiments on Monterey #1 sand in which the amplitudes of cyclic pulses were either increased or reduced during undrained loading. They found that the final pore pressure depends on the sequencing of the variable-

J. Geotech. Geoenviron. Eng., 2014, 140(12): 04014075

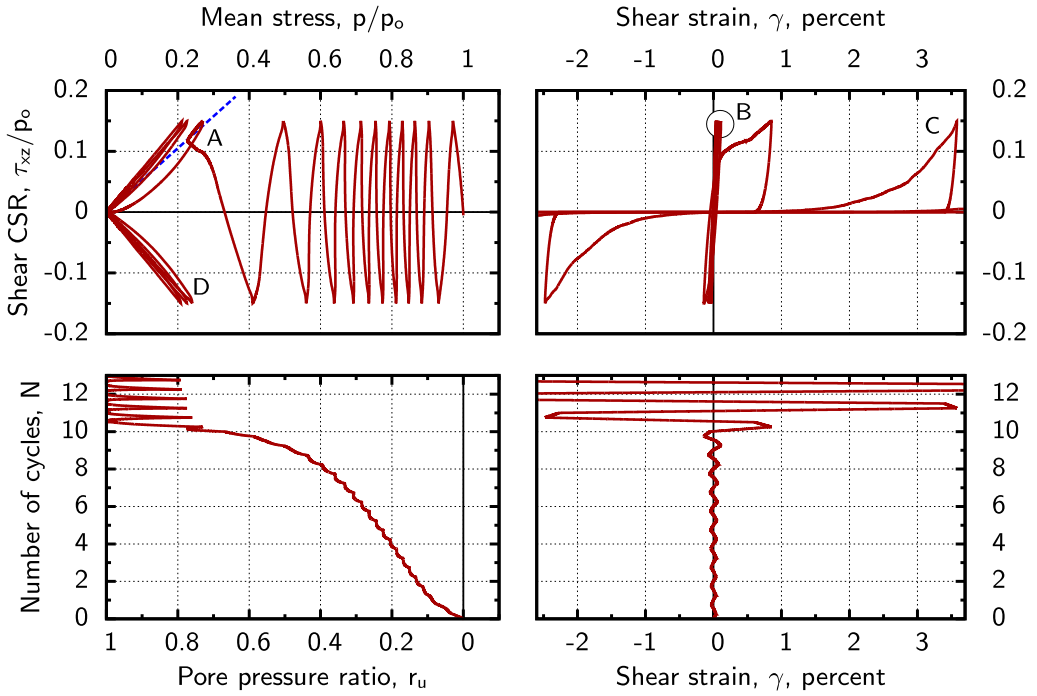

Fig. 8. DEM simulation of cyclic undrained simple shear loading: $e = 0.704$, $p_o = 80$ kPa, and $\tau_{xz} = 13$ kPa; the PT line is shown in the stress path plot as a dashed line

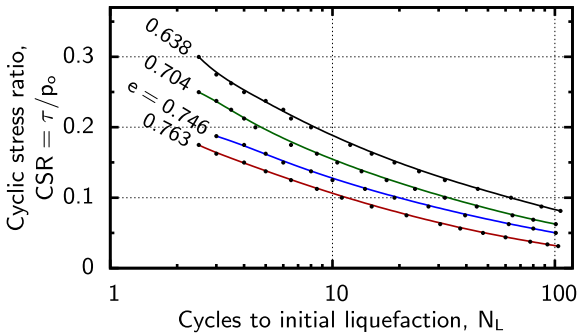

Fig. 9. Liquefaction curves of four DEM assemblies

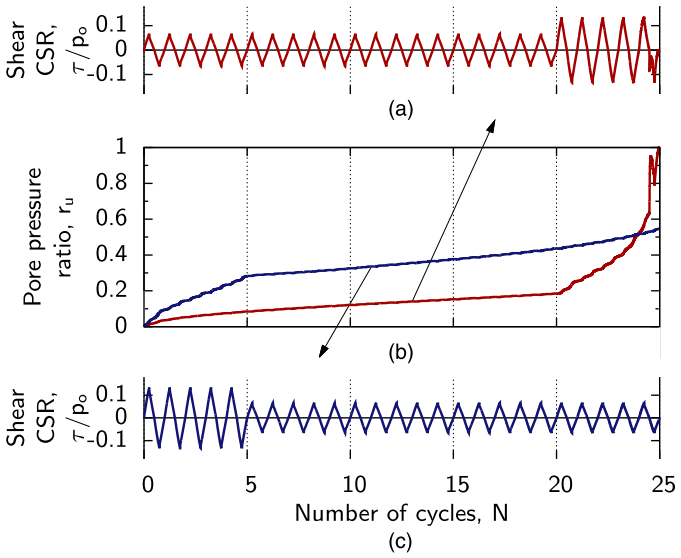

Fig. 10. Simulations of two sequences of large and small cyclic pulses ($e = 0.746$, $p_o = 80$ kPa): (a) 20 small pulses followed by five large pulses; (b) pore-pressure ratio for two sequences; (c) five large pulses followed by 20 small pulses.

amplitude cyclic pulses. This phenomenon was investigated with two types of simulations. With the first type, two sequences of 25 pulses were applied: five large-amplitude pulses were either preceded or followed by 20 small-amplitude pulses that had half the amplitude of the larger pulses (Fig. 10). For sequences with magnitudes large enough to produce significant pore pressures, it was found that the more damaging sequences started with the smaller pulses. Fig. 10 shows typical results for a loose assembly with a void ratio $e = 0.746$. Through trial and error, the reference amplitude was varied (i.e., that of the larger pulses), so that the full set of 25 pulses—20 small followed by five large—would produce initial liquefaction ($r_u = 1$), but maintaining the ratio 1:2 of pulse amplitudes (values $\tau/p_o = 0.067$ and 0.134 in Fig. 10). Once the proper reference amplitude was established, the alternative sequence was run, with the larger pulses applied first. This second sequence resulted in an r_u of only 0.546. These observations were consistent with trends described by Wang and Kavazanjian (1989). However, the difference in the effects of the two sequences was reduced with denser assemblies, and the difference was almost nonexistent with the densest assembly ($e = 0.638$).

In a second type of simulation, a modulated sequence of rising and falling stress amplitudes was applied (Fig. 11). As with all other simulations, these were strain-controlled tests in the manner of Fig. 7, in which shear strain was advanced at a constant rate $\pm\dot{\gamma}_{xz}$ until a target shear stress was reached, whereupon the strain direction was reversed. The target stress of the ith pulse was $\tau_i = \tau_{\max} \sin(\pi i/N)$ for the $N = 20$ modulated pulses, with 10 leading (rising) pulses followed by 10 trailing (falling) pulses. When the maximum stress $\tau_{\max}$ was relatively small and produced a final r_u

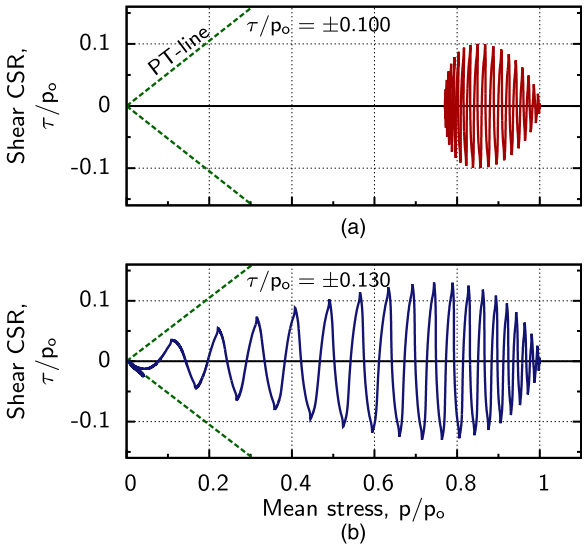

Fig. 11. Simulations with modulated sequences of cyclic pulses ($e = 0.746$, $p_o = 80$ kPa)

less than 0.5, the leading pulses were more damaging than the trailing pulses. This result is apparent in the stress path of Fig. 11(a), where the stress path is more elongated to the right. With a larger τ_{max}, the opposite trend is observed: the trailing pulses produce a larger increase in pore pressure, which results in a stress path that is elongated toward the left [Fig. 11(b)].

Seismic Loading

In a final series of simulations, 24 transient seismic loading sequences were applied to four assemblies of 6,400 particles with different void ratios. By analyzing the simulation results, a severity measure (SM) was proposed that predicts the onset of liquefaction, based on shear stress records. A suite of 24 ground motions was selected from the Next Generation Attenuation (NGA) database maintained by the Pacific Earthquake Engineering Research (PEER) Center (2000). The selected ground motions were screened from approximately 4,000 candidate motions to provide a diversity of spectral and temporal conditions as determined with four intensity measures (IMs): peak ground acceleration with a magnitude scaling factor (PGA/MSF) (Arango 1996); Arias intensity (Kayen and Mitchell 1997); cumulative absolute velocity (CAV_5) intensity (Kramer and Mitchell 2006); and normalized energy demand (NED) intensity (Green 2001). Each of the 24 motions produced a large value of one IM but a low value of another IM, all in various combinations of IM pairs, thus providing a suite of 24 motions with significantly different amplitudes, frequency contents, durations, and phasing relationships.

These ground acceleration records cannot be input directly into the DEM model. Shear-stress histories were extracted from the ground accelerations by applying these motions as inputs in an equivalent linear-wave propagation model of a 6-m sand layer using the *ProShake 1.1* software. The resulting stress histories were in the form of CSR records of shearing stress divided by the initial vertical confining stress, $\tau_{xz}/\sigma_{zz,o}$ (τ_{xz}/p_o in isotropically consolidated simulations). Rather than applying a CSR record directly, the record was processed in two ways. First, the CSR record was digitally perused to identify all of its reversals of loading direction. These peaks and valleys became the target shearing stresses at which the direction of the shearing strain $\pm\dot{\gamma}_{xz}$ was reversed while shearing with the same rate magnitude (see Fig. 7).

A second modification was applied at the start of a simulation: the stresses of each CSR record were scaled by a factor Φ so that initial liquefaction was delayed until the very end of the record. A different scaling factor Φ was required for each of the 24 CSR records, and the factors also differed among the four assemblies with different void ratios. The necessary factors were determined through a trial-and-error procedure for each of the 24 records and for each void ratio. Fig. 12 shows the results of a single scaled CSR record for a DEM assembly with a void ratio $e = 0.704$. The scaled record of CSR versus time is shown in the lower left of the plot. The factor $\Phi = 0.647$ in Fig. 12 causes the assembly to reach an $r_u = 0.932$ at the end of the record. Increasing Φ to 0.648 pushes the assembly beyond initial liquefaction, producing a few small butterfly oscillations at the end of the stress path (as in Fig. 8).

Although arriving at the proper factors Φ is a time-consuming process, this process serves three purposes:

1. The factor Φ provides a quantifiable basis for ranking the severities of the 24 original (unscaled) CSR records with respect to their propensity for producing initial liquefaction ($r_u = 1$). Specifically, the inverse of each factor, $1/\Phi$, is a measure of the severity of the particular ground motion and its shearing record (i.e., the original unscaled CSR record). The 24 records are ranked in Fig. 13, with the most severe records at the top and the most benign at the bottom. The ranking in Fig. 13 was derived from the single assembly with a void ratio $e = 704$. The scaled CSR record of Fig. 12 appears near the middle of the ranking (labeled by the open circle in Fig. 13).
2. Having scaled all 24 shear stress records so that each postponed initial liquefaction until the end of the record, a commonality in their (scaled) features is sought. That is, possible severity measures (SMs) are explored, which are defined as a scalar value derived from a CSR record that measures the record's propensity for producing initial liquefaction. For example, the peak shear stress in a CSR record (e.g., the single point A in the lower left of Fig. 12) could serve as a simple (albeit inefficient) SM. An ideal SM would have the same scalar value for each of the 24 scaled CSR records, because each record is scaled to reach a common state of initial liquefaction at the end of the record. The range of the 24 SM values for the scaled records is an indicator of the efficiency of a candidate SM. Although many candidate SMs were investigated, this work provides results for four SMs, described in the following.
3. Besides its use as a predictor of initial liquefaction, an ideal SM would also predict other damaging effects of a particular seismic record. These effects could include pore pressure rise (Δu or r_u) for CSR records that are not sufficiently severe to initiate liquefaction, postliquefaction strains for more severe records, etc.

The first and second items are addressed, and a particular SM is also applied to the prediction of pore pressure rise, as suggested in Item 3.

The key to this approach is finding the scaling factor Φ of each seismic CSR record that would postpone the onset of liquefaction until the very end of the record. For this purpose, a primary advantage of DEM simulations was used: the ability to repeatedly subject the same assembly (i.e., virtual specimen) to the 24 records, each with different scaling factors Φ, thus finding the proper factors by trial and error. Ten or 11 trials were usually necessary with each CSR record to find its Φ with a precision of ± 0.001. This same procedure was applied to all four assemblies with different void ratios.

The severities of the 24 records are shown in the slope graph of Fig. 14 for the four assemblies. In Fig. 14, the records are ranked

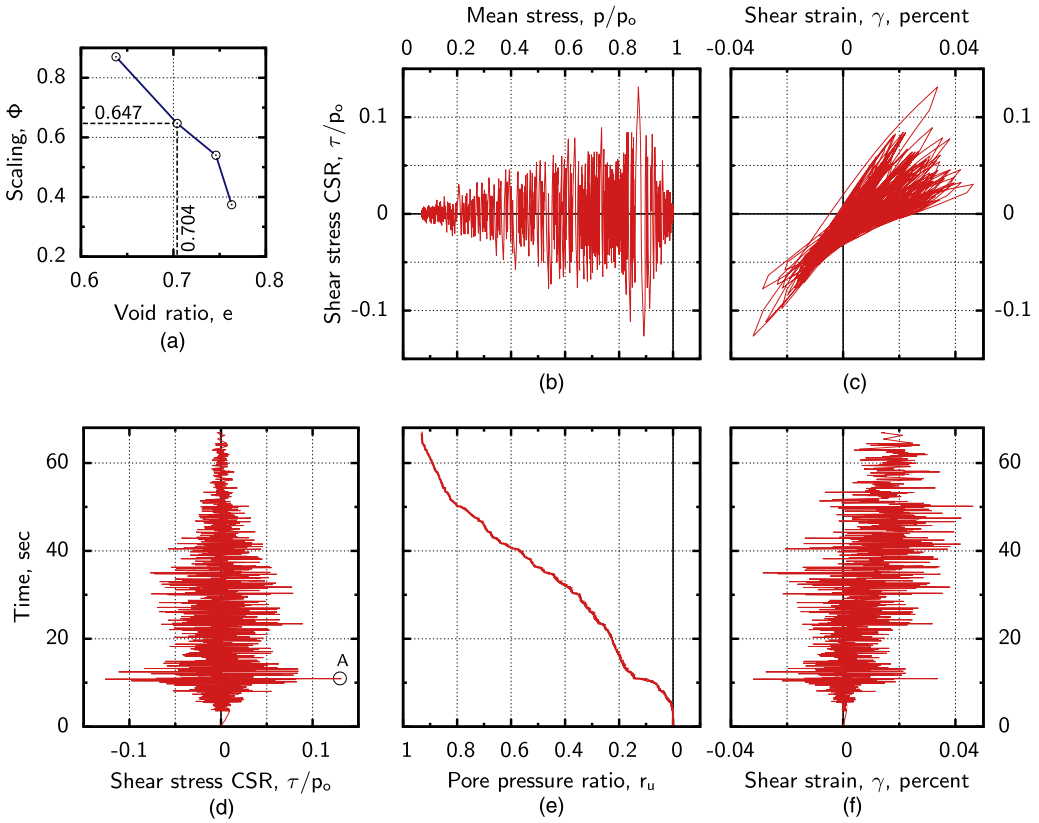

Fig. 12. Seismic loading of a DEM assembly ($e = 0.746$, $p_o = 80$ kPa); the record of CSRs (CSR $= \tau_{xz}/p_o$) is from the PEER NGA record LANDERS/MCF000; shear stresses are scaled by factor $\Phi = 0.647$ to suspend initial liquefaction until the end of the CSR record; (a) dependence of Φ on the assembly void ratio e; (b) stress path; (c) stress and strain; (d) time history of stress; (e) time history of pore-pressure ratio; (f) time history of shear strain

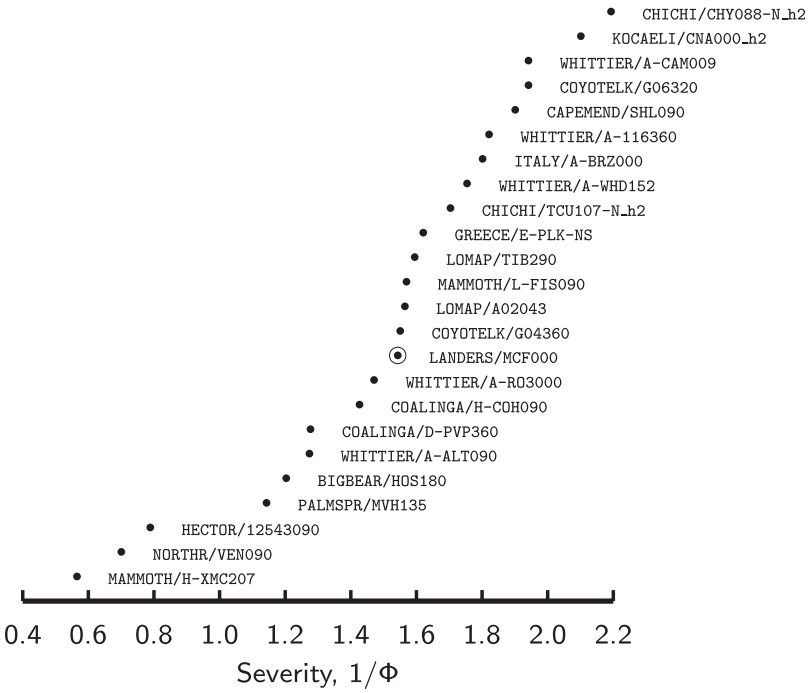

Fig. 13. Ranking of severities $1/\Phi$ of 24 seismic CSR records ($e = 0.746, p_o = 80$ kPa); records near the top are the most severe, requiring a small Φ to forestall liquefaction until the end of the record

J. Geotech. Geoenviron. Eng., 2014, 140(12): 04014075

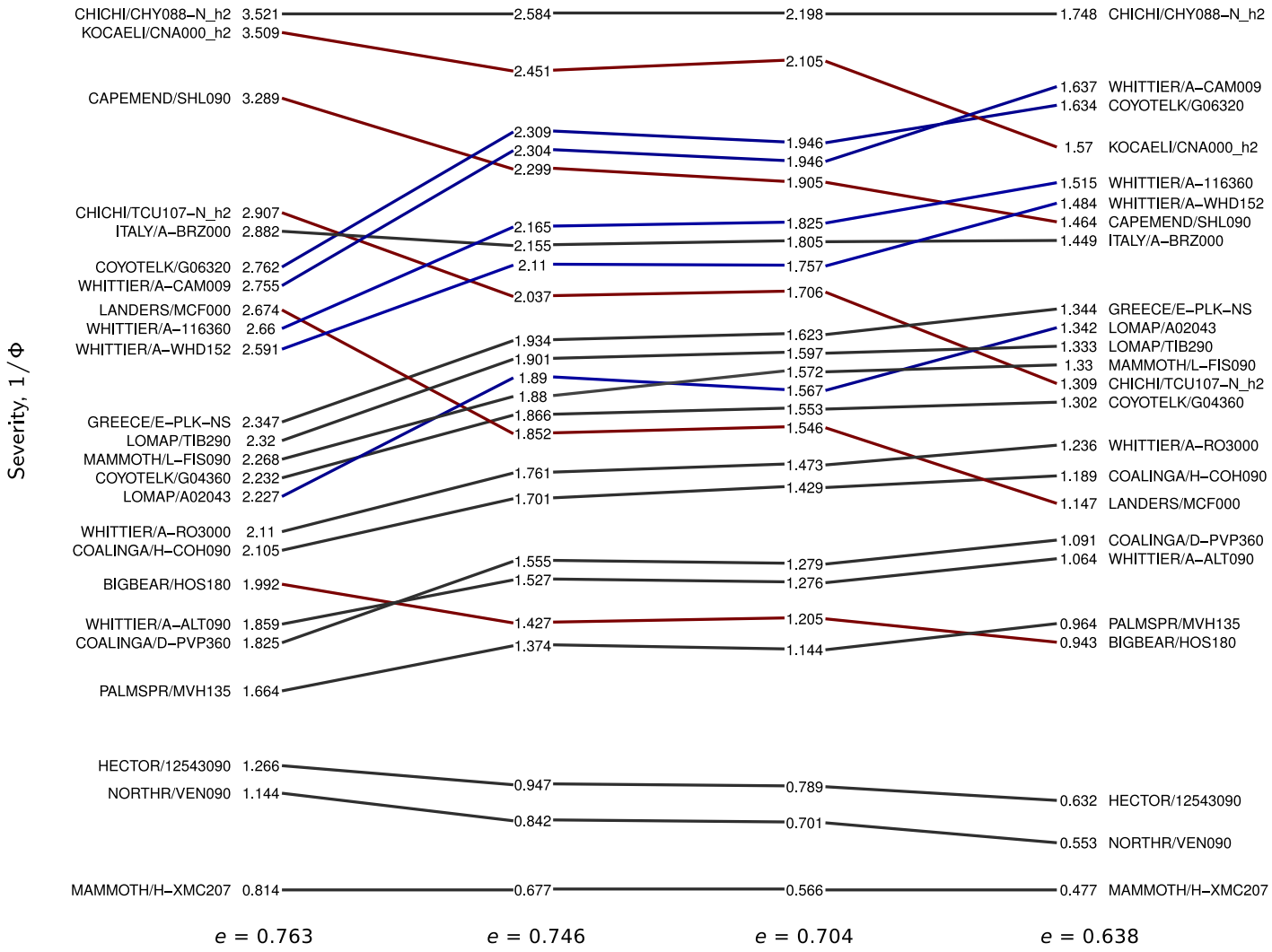

Fig. 14. Rankings of severities $1/\Phi$ of 24 seismic CSR records, based upon simulations with four densities

from the most severe (top, large $1/\Phi$) to the least severe (bottom), with the density increasing from left to right (the ranking in Fig. 13 is reproduced as the third column in Fig. 14). Because denser assemblies are more resistant to initial liquefaction, the scaling factor Φ of each CSR record must be increased with each increase in density (for example, with the CHICHI/CHY088-N_h2 record at the top of Fig. 14, the inverse factor $1/\Phi$ is reduced from 3.521 to 1.748 as the void ratio decreases from 0.763 to 0.638). The ranking of the 24 records is not consistent across the four densities, as is apparent from the crossing lines. Oddly, the severities of certain CSR records, relative to other records, decrease with increasing density, whereas the severities of other records increase relative to other records at greater density. For example, the LANDERS/MCF000 record is much more severe than the LOMAP/A02043 record when applied to the loosest assembly, but these roles are reversed with the densest assembly. This anomalous density-dependent behavior was also noted in a previous section regarding nonuniform sequences of large and small shearing pulses.

Many scalar SMs were explored as candidates for predicting the propensity of a particular CSR record for producing initial liquefaction. Four representative SMs are as follows:

$$\mathrm{SM}_1 = |\tau_{\max}/p_o| \tag{4}$$

$$\mathrm{SM}_2 = \int \frac{\tau d\gamma^{\mathrm{plastic}}}{p_o} \tag{5}$$

$$\mathrm{SM}_3 = \int H(|\gamma| - \gamma_t)|d\gamma| \tag{6}$$

$$\mathrm{SM}_4 = \int \left| d\left[\left(\frac{|\tau|}{p} \right)^2 \right] \right| = 2 \int \frac{|\tau|}{p} \left| \frac{d|\tau|}{p} - \frac{|\tau|}{p} \frac{dp}{p} \right| \tag{7}$$

which represent the maximum shear ratio of a CSR record (SM_1), a NED (SM_2), a strain-path measure (SM_3), and a stress-path measure (SM_4). For the unidirectional loading of the DEM simulations, τ is the shear stress τ_{xz}; γ is the shear strain γ_{xz}; γ_t is a threshold shear stress (assumed to be 0.01%); $H()$ is the Heaviside function, which equals zero unless the current strain magnitude $|\gamma_{xz}|$ exceeds γ_t (in which case, $H = 1$); p_o is the initial mean effective

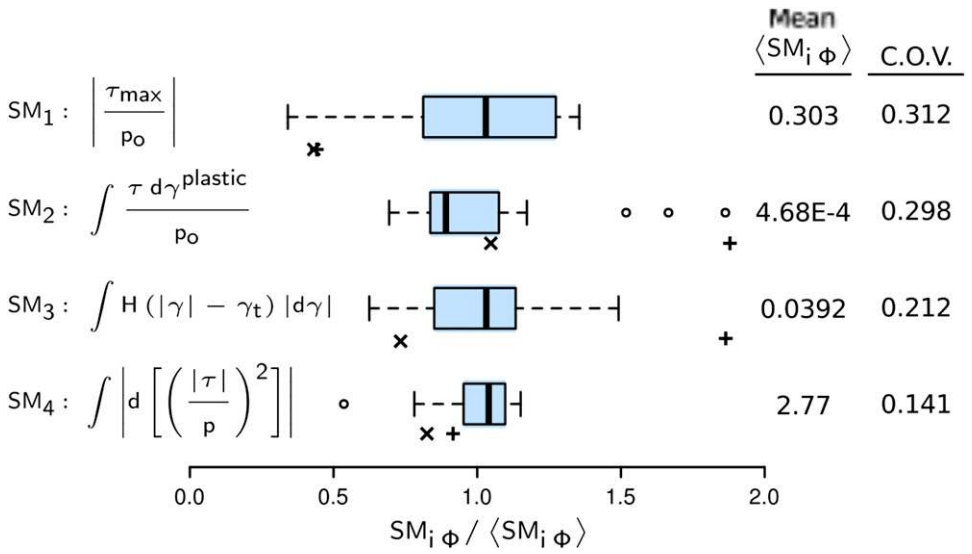

Fig. 15. Efficiencies of SMs: box plots of 24 cyclic stress records, scaled to produce initial liquefaction ($e = 0.746$, $p_o = 80$ kPa); values for the nonuniform sequence of Fig. 10(a) are marked with plus symbol; values for the sequence of Fig. 11(b) are marked with cross symbol; COV = coefficient of variation

stress; and p is the current mean effective stress. The plastic strain increment $d\gamma^{\text{plastic}}$ in Eq. (5) is computed by subtracting the elastic increment $d\tau/G_{\max}$ from the full-strain increment $d\gamma$, where modulus $G_{\max}$ is estimated with the relation given in Table 1 (row 7). Unlike earthquake IMs such as the Arias intensity, these four SMs are not based on ground motions (accelerations or velocities), but instead are integrals of the stresses and strains that result from these ground motions. The four SMs are rate independent, because time is not explicitly part of their definitions. The liquefaction resistance of sands is known to be insensitive to the loading rate (i.e., nearly independent of excitation frequency), which is consistent with the four SMs. If a time history of shear stress or strain is available, the differential quantities in Eqs. (5)–(7) can be replaced with the corresponding rate differentials, for example, $d\tau = (d\tau/dt)dt$.

These four SMs were evaluated for the 24 seismic stress (CSR) records. Each simulation yields a record of shear strain γ_{xz} and mean effective stress p, as well as the input stresses τ_{xz}, permitting evaluation of integrals Eqs. (5)–(7). As stated previously, a scaling factor Φ was determined for each CSR record that would delay initial liquefaction until the end of the record, and the resulting 24 scaled SM values corresponded to a common state of initial liquefaction ($r_u = 1$), as denoted with a subscript Φ. Fig. 15 shows box plots of the four SMs in which their values from the 24 scaled CSRs ($\text{SM}_{i\Phi}$, $i = 1, 2, 3, 4$) are normalized by dividing by the mean of the particular SM, denoted as $\langle \text{SM}_{i\Phi} \rangle$. The scatter in the simplest measure, $\text{SM}_{1\Phi}$, is considerable, indicating that maximum shear stress is a poor predictor of liquefaction. Although $\text{SM}_{2\Phi}$, $\text{SM}_{3\Phi}$, and $\text{SM}_{4\Phi}$ exhibit smaller dispersions, the stress-path measure SM_4 has the least scatter, indicating a superior efficiency in predicting initial liquefaction. The efficiencies of the four SMs are summarized in the inset of Fig. 15, giving their coefficients of variation (SD/mean), with smaller coefficients corresponding to a more efficient and less scattered severity measure. The measure SM_4 of Eq. (7) yields the lowest dispersion and serves as an efficient predictor of initial liquefaction.

Fig. 15 also shows the results of applying the four SMs to the nonuniform cyclic sequences illustrated in Figs. 10 and 11. Two of these sequences resulted in liquefaction [Fig. 10(a) and Fig. 11(b)]. Although three of the SMs were poor predictors of liquefaction (the plus and cross symbols in Fig. 15), the fourth measure SM_4 gave

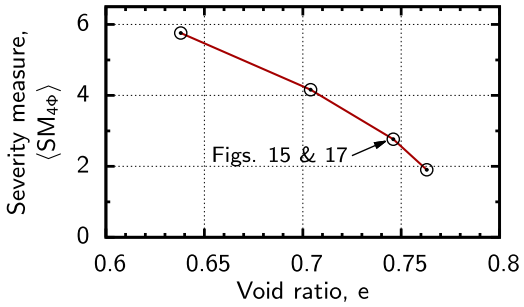

Fig. 16. Effect of specimen density on the average value of severity measure $\langle \text{SM}_{4\Phi} \rangle$ [Eq. (7)] at initial liquefaction

values close to the threshold liquefaction value $\langle \text{SM}_{4\Phi} \rangle$. In contrast, the two amplitude sequences in Fig. 10(c) did not result in liquefaction, a result that is consistent with its low SM value, $\text{SM}_4/\langle \text{SM}_{4\Phi} \rangle = 0.54$.

The value of a SM required to initiate liquefaction will depend on a soil's density. Fig. 16 gives the values of $\text{SM}_{4\Phi}$ for four specimens with different void ratios, based on the averaged results of the 24 seismic sequences. As would be expected, the value of SM_4 required to initiate liquefaction (i.e., $\text{SM}_{4\Phi}$) increases with increasing specimen density.

A proper measure of the severity of a cyclic sequence should also predict the preliquefaction rise in pore pressure. Fig. 17 shows the relationship between the excess pore pressure ratio $r_u = 1 - p/p_o$ and SM_4 for a single assembly subjected to the 24 seismic records. This SM is a monotonically increasing function of the shear stress history (scaled CSR record), which is seen to advance in a roughly linear manner with increasing pore pressure. Fig. 17 shows only modest scatter in the SM_4 versus r_u behavior, indicating that this SM would serve as an efficient predictor of pore pressure rise.

Concluding Remarks

A DEM assembly of virtual particles has been calibrated to approximate the behavior of a natural sand, particularly at small strains. This

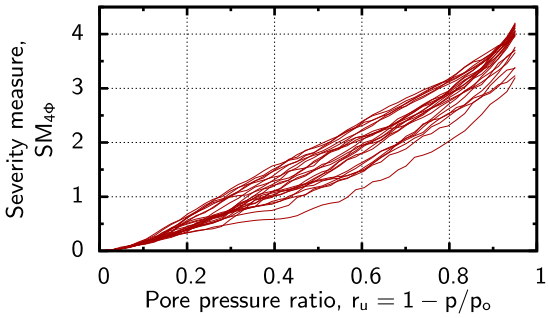

Fig. 17. Relationship between severity measure $SM_{4\Phi}$ [Eq. (7)] and excess pore pressure ratio r_u ($e = 0.746$, $p_o = 80$ kPa)

work presents simulation methodologies for exploring the complex response of such granular materials to undrained cyclic loading. Methods are also proposed for using simulations to rank the severities of different seismic sequences and for developing scalar predictors of the severity. Some anomalous behaviors have been observed, and a promising scalar predictor of liquefaction susceptibility is identified. Although laboratory tests are the final arbiter of a material's behavior, DEM simulations offer certain capabilities that are difficult to achieve in a laboratory setting; in particular, the ability to subject the same virtual assembly to nearly unlimited loading sequences.

Natural extensions of the present work would include simulations of bidirectional seismic shearing and of seismic loading in sloping-ground conditions. Even with its advantages, DEM simulations continue to be hampered by the computational demands of effectively simulating large, realistic boundary-value problems (foundations, excavations, etc.) or even conducting small element tests well into the postliquefaction regime in which the strain excursions become very large. However, discrete-element simulations can serve to investigate many important aspects of the complex cyclic behavior of soils.

Acknowledgments

This material is based upon work supported by the National Science Foundation under Grant No. NEESR-936408.

References

Agnolin, I., and Roux, J.-N. (2007). "Internal states of model isotropic granular packings. III. Elastic properties." *Phys. Rev. E: Stat. Nonlinear Soft Matter Phys.*, 76(6), 061304.

Arango, I. (1996). "Magnitude scaling factors for soil liquefaction evaluations." *J. Geotech. Engrg.*, 10.1061/(ASCE)0733-9410(1996)122:11(929), 929–936.

Arulanandan, K., and Scott, R. F. (1993). "Project VELACS—Control test results." *J. Geotech. Engrg.*, 10.1061/(ASCE)0733-9410(1993)119:8(1276), 1276–1292.

Arulmoli, K., Muraleetharan, K. K., Hossain, M. M., and Fruth, L. S. (1992). "VELACS verification of liquefaction analyses by centrifuge studies laboratory testing program: Soil data report." *Rep. No. Project No. 90-0562*, Earth Technology, Irvine, CA.

Ashmawy, A. K., Sukumaran, B., and Hoang, V. V. (2003). "Evaluating the influence of particle shape on liquefaction behavior using discrete element modeling." *Proc., 13th Int. Offshore and Polar Engineering Conf.*, Vol. 2, International Society of Offshore and Polar Engineers (ISOPE), Cupertino, CA, 542–549.

ASTM. (2006a). "Standard test methods for maximum index density and unit weight of soils using a vibratory table." *D4253-00*, West Conshohocken, PA.

ASTM. (2006b). "Standard test methods for minimum index density and unit weight of soils and calculation of relative density." *D4254-00*, West Conshohocken, PA.

Cavarretta, I., Coop, M., and O'Sullivan, C. (2010). "The influence of particle characteristics on the behaviour of coarse grained soils." *Géotechnique*, 60(6), 413–423.

Cho, G.-C., Dodds, J., and Santamarina, J. C. (2006). "Particle shape effects on packing density, stiffness, and strength: Natural and crushed sands." *J. Geotech. Geoenviron. Eng.*, 10.1061/(ASCE)1090-0241(2006)132:5(591), 591–602.

Cole, D. M., Mathisen, L. U., Hopkins, M. A., and Knapp, B. R. (2010). "Normal and sliding contact experiments on gneiss." *Granular Matter*, 12(1), 69–86.

Dobry, R., and Ng, T.-T. (1992). "Discrete modelling of stress-strain behaviour of granular media at small and large strains." *Eng. Comput.*, 9(2), 129–143.

Duku, P. M., Stewart, J. P., Whang, D. H., and Yee, E. (2008). "Volumetric strains of clean sands subject to cyclic loads." *J. Geotech. Geoenviron. Eng.*, 10.1061/(ASCE)1090-0241(2008)134:8(1073), 1073–1085.

El Shamy, U., and Zamani, N. (2012). "Discrete element method simulations of the seismic response of shallow foundations including soil-foundation-structure interaction." *Int. J. Numer. Anal. Methods Geomech.*, 36(10), 1303–1329.

El Shamy, U., and Zeghal, M. (2005). "Coupled continuum-discrete model for saturated granular soils." *J. Eng. Mech.*, 10.1061/(ASCE)0733-9399(2005)131:4(413), 413–426.

Goddard, J. D. (1990). "Nonlinear elasticity and pressure-dependent wave speeds in granular media." *Proc. R. Soc. London, Ser. A*, 430(1878), 105–131.

Green, R. A. (2001). "Energy-based evaluation and remediation of liquefiable soils." Ph.D. dissertation, Virginia Tech, Blacksburg, VA.

Hakuno, M., and Tarumi, Y. (1988). "A granular assembly simulation for the seismic liquefaction of sand." *Proc. J. Soc. Civ. Eng.*, 398(10), 129–138.

Hardin, B. O. (1978). "The nature of stress-strain behavior for soils." *Proc., ASCE Geotechnical Engineering Division Specialty Conf.: Earthquake Engineering and Soil Dynamics*, Vol. 1, ASCE, New York, 3–90.

Ibsen, L. B. (1999). "The mechanism controlling static liquefaction and cyclic strength of sand." *Physics and mechanics of soil liquefaction*, P. V. Lade and J. A. Yamamuro, eds., Balkema, Rotterdam, Netherlands, 29–39.

Jäger, J. (1999). "Uniaxial deformation of a random packing of particles." *Arch. Appl. Mech.*, 69(3), 181–203.

Jäger, J. (2005). *New solutions in contact mechanics*, WIT Press, Southampton, U.K.

Kammerer, A. M., Wu, J., Pestana, J. M., Riemer, M., and Seed, R. B. (2000). "Cyclic simple shear testing of Nevada Sand for PEER Center project 2051999." *Geotechnical Engineering Rep. UCB/GT/00-01*, Dept. of Civil and Environmental Engineering, Univ. of California at Berkeley, Berkeley, CA.

Kayen, R. E., and Mitchell, J. K. (1997). "Assessment of liquefaction potential during earthquakes by Arias intensity." *J. Geotech. Geoenviron. Eng.*, 10.1061/(ASCE)1090-0241(1997)123:12(1162), 1162–1174.

Kramer, S. L., and Mitchell, R. A. (2006). "Ground motion intensity measures for liquefaction hazard evaluation." *Earthquake Spectra*, 22(2), 413–438.

Kuhn, M. R. (2002). "OVAL and OVALPLOT: Programs for analyzing dense particle assemblies with the discrete element method." ⟨http://faculty.up.edu/kuhn/oval/oval.html⟩ (Aug. 28, 2014).

Kuhn, M. R. (2011). "Implementation of the Jäger contact model for discrete element simulations." *Int. J. Numer. Methods Eng.*, 88(1), 66–82.

Mindlin, R. D., and Deresiewicz, H. (1953). "Elastic spheres in contact under varying oblique forces." *J. Appl. Mech.*, 19(1), 327–344.

Mitchell, J. K., and Soga, K. (2005). *Fundamentals of soil behavior*, 3rd Ed., Wiley, Hoboken, NJ.

Ng, T.-T., and Dobry, R. (1994). "Numerical simulations of monotonic and cyclic loading of granular soil." *J. Geotech. Engrg.*, 10.1061/(ASCE)0733-9410(1994)120:2(388), 388–403.

O'Sullivan, C., Cui, L., and Bray, J. D. (2004). "Three-dimensional discrete element simulations of direct shear tests." *Proc., 2nd Int. PFC Symp.: Numerical Modeling in Micromechanics via Particle Methods*,

Y. Shimizu, R. Hart, and P. Cundall, eds., Taylor & Francis, London, 373–382.
Pacific Earthquake Engineering Research (PEER) Center. (2000). "PEER strong motion database." ⟨http://peer.berkeley.edu/smcat⟩ (Aug. 28, 2014).
Pestana, J. M., and Whittle, A. J. (1995). "Compression model for cohesionless soils." *Géotechnique*, 45(4), 611–631.
Porcino, D., and Caridi, G. (2007). "Pre- and post-liquefaction response of sand in cyclic simple shear." *Proc., Geo-Denver 2007: New Peaks in Geotechnics*, M. M. Dewoolkar and J. P. Koester, eds., ASCE, Reston, VA, 1–10.
ProShake 1.1 [Computer software]. Redmond, WA, EduPro Civil Systems.
Salot, C., Gotteland, P., and Villard, P. (2009). "Influence of relative density on granular materials behavior: DEM simulations of triaxial tests." *Granular Matter*, 11(4), 221–236.
Santamarina, C., and Cascante, G. (1998). "Effect of surface roughness on wave propagation parameters." *Géotechnique*, 48(1), 129–136.
Sazzad, M. M., and Suzuki, K. (2010). "Micromechanical behavior of granular materials with inherent anisotropy under cyclic loading using 2D DEM." *Granular Matter*, 12(6), 597–605.
Simmons, G., and Brace, W. F. (1965). "Comparison of static and dynamic measurements of compressibility of rocks." *J. Geophys. Res.*, 70(22), 5649–5656.
Sitharam, T. G. (2003). "Discrete element modelling of cyclic behaviour of granular materials." *Geotech. Geol. Eng.*, 21(4), 297–329.
Thornton, C., and Antony, S. J. (1998). "Quasi-static deformation of particulate media." *Phil. Trans. Roy. Soc. Lond. A*, 356(1747), 2763–2782.
Walton, K. (1987). "The effective elastic moduli of a random packing of spheres." *J. Mech. Phys. Solids*, 35(2), 213–226.
Wang, J. N., and Kavazanjian, E., Jr. (1989). "Pore pressure development during non-uniform cyclic loading." *Soils Found.*, 29(2), 1–14.
Wichtmann, T., and Triantafyllidis, T. (2009). "Influence of the grain-size distribution curve of quartz sand on the small strain shear modulus G_{max}." *J. Geotech. Geoenviron. Eng.*, 10.1061/(ASCE)GT.1943-5606.0000096, 1404–1418.
Zettler, T. E., Frost, J. D., and DeJong, J. T. (2000). "Shear-induced changes in smooth HDPE geomembrane surface topography." *Geosynth. Int.*, 7(3), 243–267.